V International Conference on Computational Methods in Marine Engineering
MARINE 2013
B. Brinkmann and P. Wriggers (Eds)

AXISYMMETRIC TRANSIENT MODELLING OF A WIND TURBINE FOUNDATION IN COHESIONLESS SOIL USING THE PREVOST'S MODEL

B. CERFONTAINE*,†, S. LEVASSEUR† AND R. CHARLIER†

*FRIA, FRS-FNRS, National Fund for Scientific Research
Brussels, Belgium
e-mail: b.cerfontaine@ulg.ac.be

† Geomechanics and Geological Engineering
Department ArGEnCo, University of Liege
Sart-Tilman, Liege, Belgium

Key words: Prevost's Model, Suction Caisson, Constitutive Law

Abstract. Suction caissons are more and more used for offshore foundations. This paper deals with the cyclic modelling of suction caissons using the Prevost's model. The case study is a 8m large diameter caisson embedded in dense No. 0 Lundsand. Parameters for the model are calibrated using drained triaxial tests. A parametric study concerning the influence of the constitutive law, the skirt length and permeability is carried out.

1 INTRODUCTION

Nowadays, offshore power plants are gathering momentum [1]. Developers are planning new wind farms in deeper waters and further away from the coasts for economical and environmental purpose as well. Wind turbines are growing in size and power, increasing the foundation requirements. Developing an accurate design approach is a crucial issue for private companies that aim to decrease building costs. Foundation costs may represent up to 30 % of the total [2]!

Suction caissons are a serious alternative to piling for offshore structures. These are lighter, easier to install and cheaper than classical foundations [3]. The caisson is set up by reducing the water pressure inside the bucket by pumping. The differential pressure on the top of the caisson induces a downward force that digs the foundation into the soil.

Numerical modelling of this kind of offshore foundations is not trivial. Simple numerical models exist, based on in-situ test measurements, semi-empirical methods or macro-elements [3, 4, 5, 6]. Classical isotropic-hardening models are not able to truly represent the cyclic loading paths which involve elastic and plastic deformations in both loading and unloading cases. One should consider more sophisticated models such as the Prevost's

model [7] which is dedicated to represent cyclic behaviour of cohesive or frictionless soils. An improved version of this model is available in [8] in the scope of earthquake modelling. An application to offshore gravity structures is available in [9] for cohesive soil.

The Prevost's model is applied in this paper to a suction caisson case study to highlight the main features of the cyclic loading of offshore foundations. The main objective is to test the possibilities and limitations of the model for this purpose. A parametric study is carried out on both skirt length and permeability.

2 THE PREVOST'MODEL

2.1 Definitions

The sign convention of soil mechanics is adopted : compressive stresses and strains are positive. The Macauley brackets $\langle\rangle$ are defined according to

$$\langle f \rangle = \begin{cases} 0, & f < 0 \\ f, & f \geq 0 \end{cases} \tag{1}$$

The symbol":" indicates a dot product between two tensors (in bold characters). For example, if $\boldsymbol{\sigma'}$ is the effective (Cauchy) stress tensor, the product $\boldsymbol{\sigma'} : \boldsymbol{\sigma'} = \sigma_{ij} \cdot \sigma_{ij}$ in index notation. The identity tensor is written $\boldsymbol{\delta}$, then the mean effective stress is defined as $p' = 1/3 \cdot \boldsymbol{\sigma'} : \boldsymbol{\delta}$. The deviatoric stress tensor and the invariant of deviatoric stresses are defined through

$$\mathbf{s} = \boldsymbol{\sigma'} - p' \cdot \boldsymbol{\delta} \qquad \text{and} \qquad \mathrm{q} = \sqrt{\frac{3}{2} \cdot \mathbf{s} : \mathbf{s}} \tag{2}$$

2.2 Constitutive equations

The Prevost's model lies within the framework of elasto-plasticity. Constitutive equations are written in incremental form. The equation below links the effective stress rate $\dot{\boldsymbol{\sigma}}'$ to the elastic deformation rate $\dot{\boldsymbol{\epsilon}} - \dot{\boldsymbol{\epsilon}}^p$

$$\dot{\boldsymbol{\sigma}}' = \mathbf{E} : \dot{\boldsymbol{\epsilon}} - \dot{\boldsymbol{\epsilon}}^p \tag{3}$$

where $\mathbf{E}$ is the fourth-order tensor of elastic coefficients, $\dot{\boldsymbol{\epsilon}}$ is the total deformation rate and $\dot{\boldsymbol{\epsilon}}^p$ is the plastic deformation rate defined through

$$\dot{\boldsymbol{\epsilon}}^p = \mathbf{P} \cdot \langle \mathrm{L} \rangle \tag{4}$$

$\mathbf{P}$ is a symmetric second-order tensor defining a non-associated plastic potential. The plastic loading function, L, is a scalar that depicts the amount of plasticity deformation and is defined in the following

$$\mathtt{L} = \frac{1}{\mathrm{H'}} \cdot \mathbf{Q} : \dot{\boldsymbol{\sigma}}' \tag{5}$$

where $\mathbf{Q}$ is a second-order tensor defining the unit outer normal to the yield surface and H' the plastic modulus associated to this surface. This normal tensor can be decomposed into its deviatoric and volumetric part as

$$\mathbf{Q} = \mathbf{Q}' + \mathrm{Q"} \cdot \boldsymbol{\delta} \tag{6}$$

2.3 Yield functions

The model is made of conical nested yield surfaces in principal stress space [7]. Their apex is fixed at the origin of axes but could be translated on the hydrostatic axis to take cohesion into account if necessary. The i-th surface is the locus of the stress states that verify

$$\mathrm{f}^i \equiv \frac{3}{2} \cdot \left(\mathbf{s} - \mathrm{p}' \cdot \boldsymbol{\alpha}^i\right) : \left(\mathbf{s} - \mathrm{p}' \cdot \boldsymbol{\alpha}^i\right) - \left(\mathrm{p}' \cdot \mathrm{M}^i\right)^2 = 0 \tag{7}$$

where $\boldsymbol{\alpha}^i$ is a kinematic deviatoric stress tensor defining the coordinates of the yield surface centre in deviatoric space and M^i is a material parameter denoting the aperture of the cone.

2.4 Plastic flow rule

The plastic potential $\mathbf{P} = \mathbf{P}' + \mathrm{P}" \cdot \boldsymbol{\delta}$ is decomposed into its deviatoric part which is associative

$$\mathbf{P}' = \mathbf{Q}' \tag{8}$$

and its volumetric part which is non-associative

$$\mathrm{P}" = \frac{1}{3} \cdot \frac{\eta^2 - \bar{\eta}^2}{\eta^2 + \bar{\eta}^2} \qquad \text{where} \qquad \eta = \frac{\sqrt{3/2 \cdot \mathbf{s} : \mathbf{s}}}{\mathrm{p}'} = \frac{\mathrm{q}}{\mathrm{p}'} \tag{9}$$

The material parameter $\bar{\eta}$ takes into account the phase transformation line defined by Ishihara [10]. This parameter rules the dilationnal behaviour and separates the p'-q plane into two zones. Stress ratios (η) lower than $\bar{\eta}$ indicate a plastic contractive behaviour whilst the other zone depicts a dilative plastic behaviour.

2.5 Hardening rule

The hardening rule of the surfaces is purely kinematic. During loading, the active surface moves up to come into contact with the next one. All surfaces inside the active one stay tangential at the current stress state. The relationship between plastic function and kinematic hardening is determined through the consistency condition [7] and leads to

$$\mathrm{p}' \cdot \boldsymbol{\alpha}^i = \frac{\mathrm{H}'}{\mathbf{Q}' : \boldsymbol{\mu}} \cdot \langle \mathrm{L} \rangle \cdot \boldsymbol{\mu} \tag{10}$$

where $\boldsymbol{\mu}$ is a tensor defining the direction of translation of the active surface in the deviatoric space. At this step, any direction of translation could be used depending on the strategy used to integrate the constitutive law (explicit or implicit). The only requirement is that the outermost activated surface has to be at most tangential to the next one, at the end of a given step. Overlapping of the surfaces is then avoided. In this paper, an implicit integration is adopted.

3 CALIBRATION

According to [7], calibrating the model only requires drained triaxial tests (both compressive and extensive curves are needed). Then the tensorial equation (7) describing each yield surface is simplified into

$$\mathrm{f}^i \equiv \left(\mathrm{q} - \mathrm{p}' \cdot \beta^i\right)^2 - \left(\mathrm{m}^i \cdot \mathrm{p}'\right)^2 = 0 \tag{11}$$

and the procedure of calibration is thus straightforward. Firstly, the compression q-ϵ_y curve is delineated into segments along which a plastic modulus is constant. Each transition from a segment to another gives the inital upper bound ($u^i > 0$) of each yield surface. Secondly, the same procedure is carried out for extension curves. Plastic moduli associated with each surface are still known and but initial lower bounds ($l^i < 0$) of surfaces aren't. Then, initial positions (β^i) and sizes (m^i) of the surfaces can be computed

$$m^i = \frac{u^i - l^i}{2} \qquad \beta^i = l^i + m^i \tag{12}$$

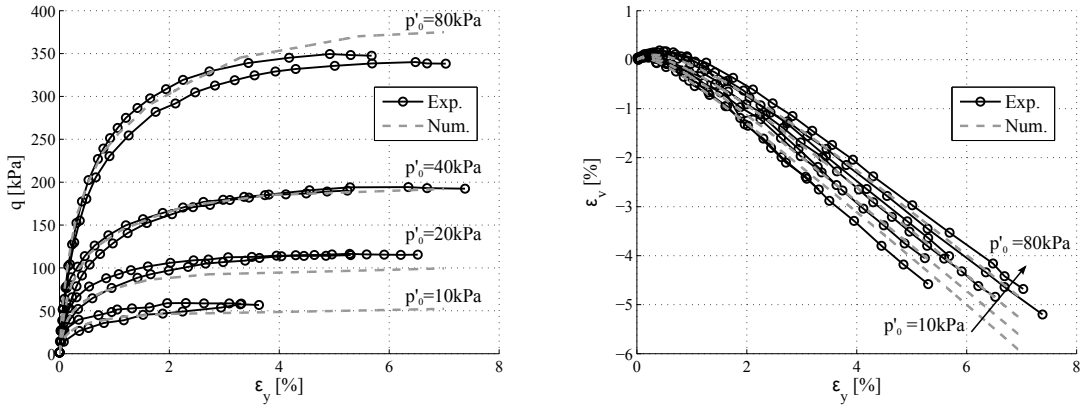

(a) q-ϵ curve (b) $\epsilon_v - \epsilon_y$ curve

Figure 1: Experimental (from [11]) and numerical drained triaxial compressive tests on Lund sand No. 0 at different initial mean effective stress (p'_0).

In the scope of this study, test on Lund sand No 0 at high relative density (around 90%, mass density of grains = $\rho_s = 2650$ kg/m^3) are assumed to represent seabed. Data are obtained from triaxial tests given in [11]. The $\mathrm{p}'_0 = 40$kPa curve is adopted as reference curve for calibration (see in Figure 1(a) and 1(b)). Unfortunately, these tests only involve compression curves. Then to characterize the soil behaviour in extension, we formulate a hypothesis We consider that behaviour in extension is similar to behaviour in compression but with a weaker resistance (as shown in [12]). The extension curve of the soil is thus assumed to be the compressive one scaled to a factor 2/3. Plastic parameters identified for the model are given in the Table 1. A dependency of stiffness on the mean effective stress is taken into account through the following relations

$$\mathrm{X}(\mathrm{p}') = \mathrm{X}_0 \cdot \left(\frac{\mathrm{p}'}{\mathrm{p}_{ref}}\right)^{\mathrm{n}} \qquad \text{where} \qquad \mathrm{X} = [\mathrm{G}, \mathrm{K}, \mathrm{H}'] \qquad \text{and} \qquad \mathrm{p}_{ref} = 100\mathrm{kPa} \tag{13}$$

The reference shear and bulk moduli are taken equal to 47MPa and 65MPa respectively. The permeability of the soil is assessed equal to 10^{-5} m/s, [3].

Table 1: Parameters describing the soil for the Prevost's model : initial position of the surfaces (α), aperture of the surfaces (M), reference plastic modulus associated (H'_0), parameter defining the volumetric plastic potential ($\bar{\eta}$), n for the dependency of stiffness on the mean effective stress.

Surf. Nb.	1	2	3	4	5	6
$\alpha[-]$	0.0917	0.1333	0.1583	0.1750	0.200	0.2250
M [−]	0.4583	0.6667	0.7917	0.8750	1.0000	1.1250
H'_0 [MPa]	50	30	20	12	5	2.5
Surf. Nb.	7	8	9	10	11	12
$\alpha[-]$	0.2467	0.2583	0.2733	0.2850	0.2950	0.3033
M [−]	1.2333	1.2917	1.3667	1.4250	1.4750	1.5167
H'_0 [MPa]	1.2	0.8	0.4	0.3	0.1	0.025
$\bar{\eta}$	1.15					
n	0.5					

4 CASE STUDY

4.1 Geometry

The case study adopted here is the modelling of a suction's caisson part of a tripod foundation in shallow water. This paper focuses on the soil behaviour and the superstructure is not modelled, nor the part of the foundations into the sea. The suction caisson is a half cylinder of 8m diameter. To a first approximation, the horizontal load is neglected and the foundation can be idealized as an axisymmetric case (see in Figure 2). The soil modelled is a 24m long times 22m high rectangular domain. The horizontal boundary at the top as well as the outermost vertical one are considered drained. In this case study, the soil and the caisson are considered perfectly stuck. The initial coefficient of lateral earth pressures is assumed to be equal to 0.7. The first metre of soil of the sea bed is not modelled and is replaced by a 10kPa confinement. A small cohesion of 2.5kPa is added to parameters calibrated above for numerical purpose.

4.2 Loading

The design of the suction caisson is based on the bearing capacity procedure developed in [15]. Then the acting vertical forces are estimated. The first step consists in applying

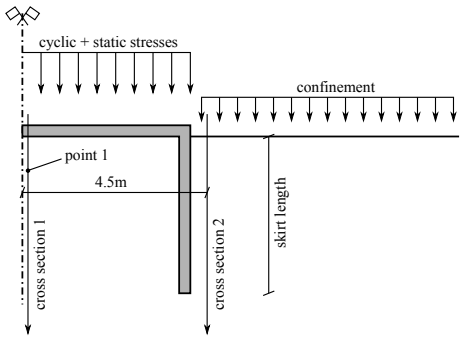

Figure 2: Geometry of the foundation. The first cross section is under the centre of the caisson, the second one is 0.5m outside the caisson. The point no 1 is located 0.5m under the centre of the caisson.

the dead weight of the wind turbine and foundation following a drained stress path. The second step concerns the cyclic loading.

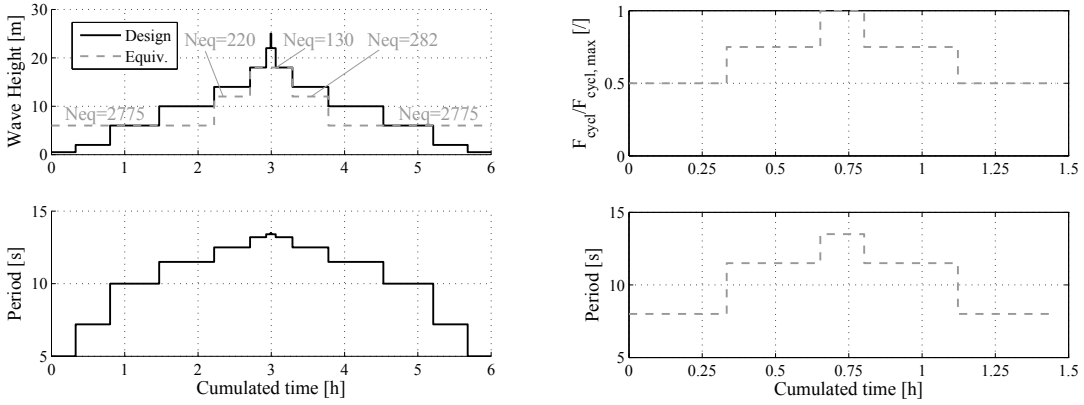

(a) Histogram for the 100-year design and equivalent storm for the Ekofisk site [13].

(b) Equivalent vertical cyclic loading adopted for the modelling of suction caisson.

Figure 3: Equivalent cyclic loading of the foundation

During a storm, waves and wind are random processes that involve a loading on the wind turbine. They don't necessary have the same principal direction nor frequency content. Then their action on the wind turbine eventually entails a loading of the suction caisson which depends on the structural response of the wind turbine.

Describing the characteristics of waves requires two components : their heights and periods [13]. The typical content of a storm can be limited to different classes of waves of given height and period. In the normal course of a storm, waves of small height and period are followed by waves of higher and higher height and period. Following this tendency, [13] obtained an equivalent cyclic loading on the soil for the 100-year design storm for the Ekofisk site (see in Figure 3(a)), based on work of [14]. Firstly, the storm is decomposed

in successive wave packets of a given height (see in Figure 3(a)). Afterwards, this loading is transformed into an equivalent number of cycles of a given shear amplitude in the soil.

In order to simplify the loading, a similar procedure is followed. The synthetic cyclic loading adopted is made of different stages of increasing amplitude and period of vertical stresses then followed by a symmetric effect of decreasing amplitude and period, see in Figure 3(b). The static vertical stress is estimated to 80 kPa while the cyclic maximal vertical stress is chosen equal to 40 kPa.

5 RESULTS

Results consist in a parametric study on factors affecting the response of the suction caisson to a cyclic loading. The influence of the constitutive law, the skirt length and the permeability, are investigated. They are provided either in a cross section for a fixed time step or at a fixed point for every time step (see in Figure 2).

5.1 Constitutive law

The first parameter investigated is the constitutive law (see in Figure 6). This first comparison shows clearly that at the beginning of a new wave packet, the effect of the elasto-plastic constitutive law is to shift the curve of pore pressure variation to greater values, probably due to contractancy of the soil. However, the influence of the contractancy seems limited to the first 10-15 metres of the soil where deviatoric stresses are of greater importance. Downwards the elasto-plastic curves tend to elastic ones and nearly become symmetric.

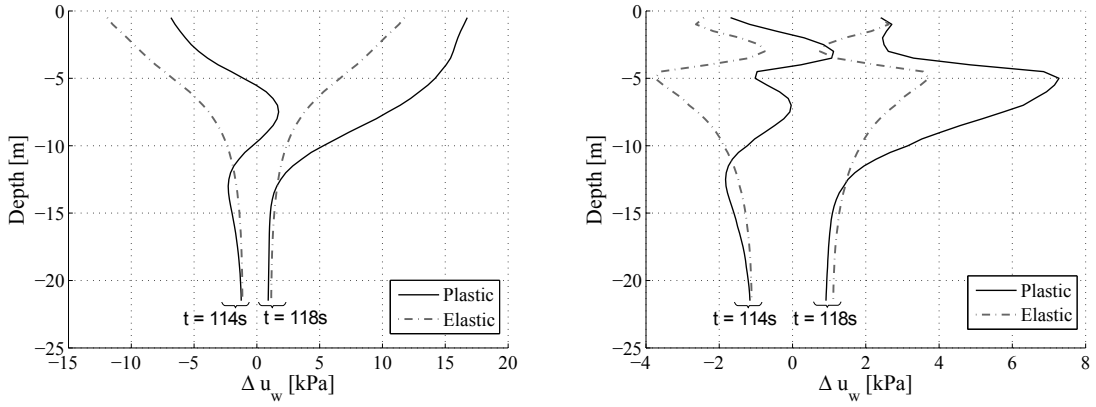

(a) Elastic/Elasto-Plastic constitutive law : variations in water pore pressure (cross section 1)

(b) Elastic/Elasto-Plastic constitutive law : variations in water pore pressure (cross section 2)

Figure 4: Cross section of the variations in pore water pressure for minimum (t= 114s) and maximum (t= 118s) vertical stresses, during the first wave packet.

5.2 Skirt length

Figure 5 depicts cross sections of pore pressure variations and mean effective stress at the beginning of the storm (first wave packet). The time steps $t = 114$s and $t = 118$s correspond to a half period where the cyclic amplitude is respectively minimum and maximum.

These figures summarize the two main effects of the skirt length. Firstly, the length of the skirt modifies the flow regime around the caisson. A higher skirt length implies a greater time to dissipate pore pressure generated at its top. On the other hand, the soil inside the caisson is confined, hence the stress ratio ($\eta = q/p'$) decreases with depth up to a reversal point (see in Figure 5(b)). This point lies at a depth slightly deeper than the skirt length. Downwards a local peak in stress ratio is clearly visible where the deviatoric stresses develop. The skirt length affects both the position and the sharpness of the local peak in η. Therefore, depending on its value, a contractive or dilative volumetric behaviour appears hence a pore pressure generation or dissipation.

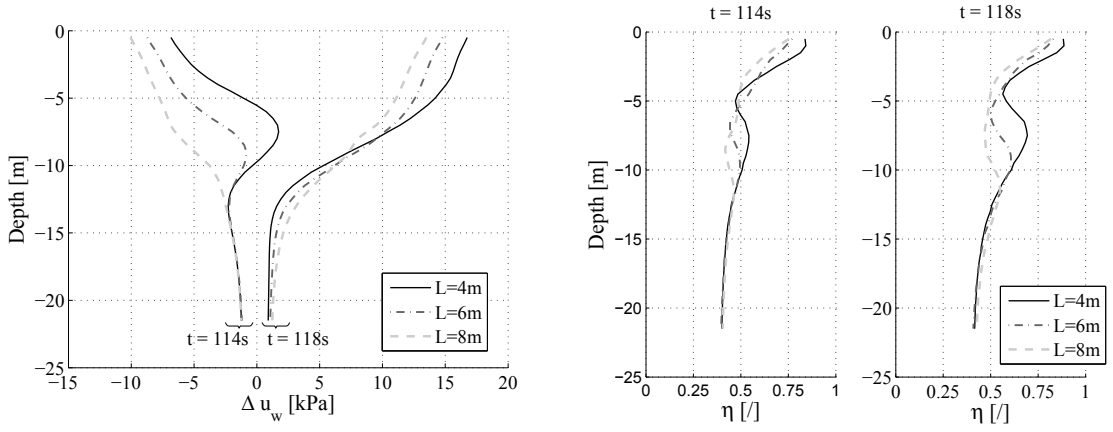

(a) Variations in water pore pressure

(b) Variations in stress ratios $\eta = q/p'$

Figure 5: Influence of the skirt length : cross section 1 for minimum (t= 114s) and maximum (t= 118s) vertical stresses, during the first wave packet.

The higher the skirt length the lower the plasticity around the soil (see in Figure 5(b)). As a consequence the shift of the curve of pore pressure variation (5(a)) is lower and the local peak is smoothed. The curve for a 8m skirt length tends to the symmetric elastic distribution.

It's worth noting that outside the caisson (cross section 2), the soil is highly plastified (see in Figure 6(b)). Indeed, due to the hypothesis of sitcky contact between the soil and the caisson, high deviatoric stresses develop whilst the mean effective stress is weak. This implies a greater shift of the pore pressure curve compared with an elastic curve (see in Figures 4(b) and 6(a)). This effect is smoothed again by the skirt depth.

The evolution of pore pressure variations in time at point 1 is given in Figure 7(a).

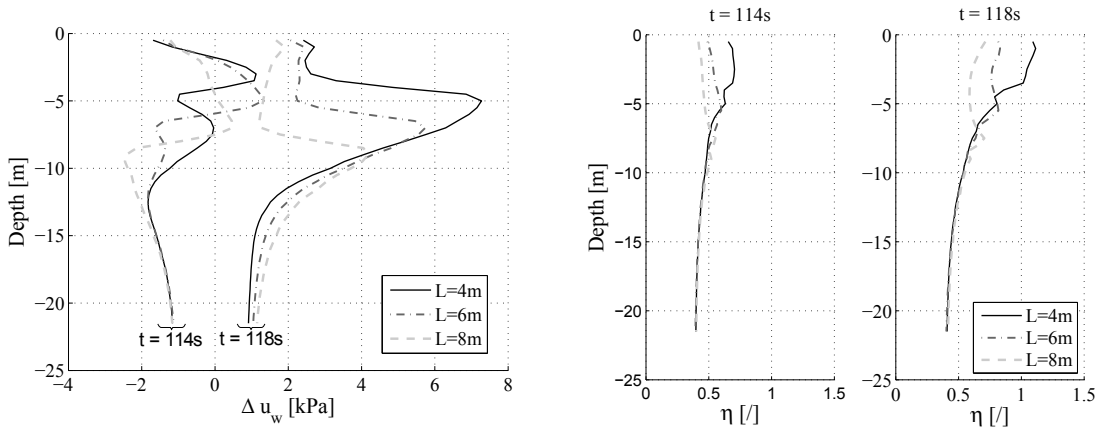

(a) Variations in water pore pressure

(b) Variations in stress ratios $\eta = q/p'$

Figure 6: Influence of the skirt length : cross section 2 for minimum (t= 114s) and maximum (t= 118s) vertical stresses, during the first wave packet.

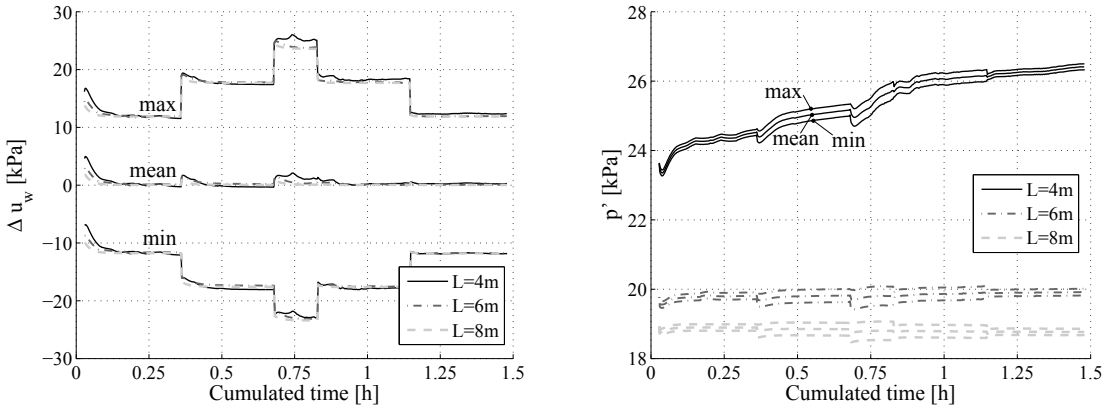

(a) Variations in water pore pressure : mean tendency and envelop curve.

(b) Mean effective stress : mean tendency and envelop curve.

Figure 7: Influence of the skirt length : evolution of pore pressure variation and mean effective stress with time at point 1.

All the curves depict the same behaviour. During the two first wave packets of the storm ($\sigma_{v,cycl} = 0.5/0.75 \cdot \sigma_{v,cycl,max}$), the pore pressure variation firstly rises up to a peak, then decreases and stabilizes. The symmetric effect is clearly visible in Figure7(b) that depicts the variations of mean effective stresss.

During the stabilized phase, the pore pressure created during cycle is dissipated within the same cycle [16]. The mirror effect of the mean effective stress is a tendency to increase as the volumetric deformation rises up and the soil densifies. Accumulation of vertical permanent displacement is greater during the transient than during the stationary phase (see in Figure8(a)). It's worth noting that the transient behaviour coupled with greater

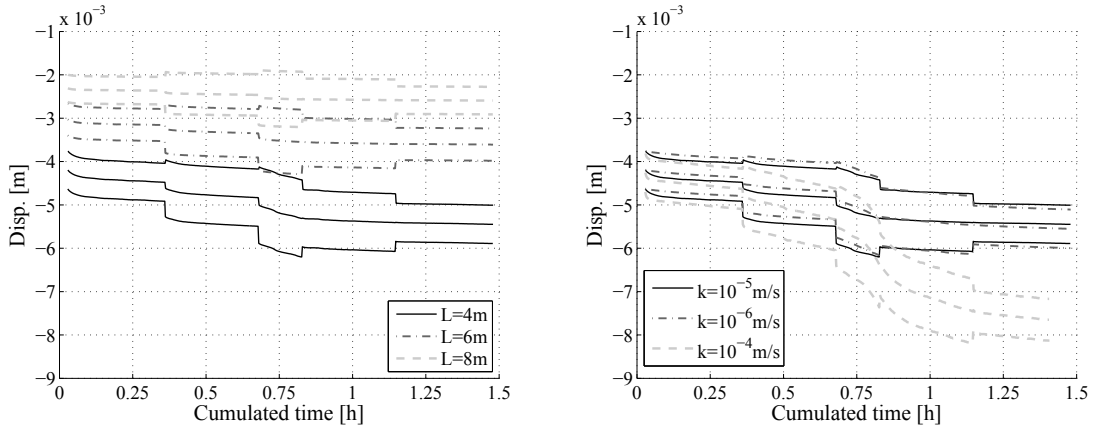

(a) Dependency on the skirt length : mean tendency and envelop curve.

(b) Dependency on the permeability : mean tendency and envelop curve.

Figure 8: Evolution of the displacement with time at point 1.

displacement accumulation disappears for the steps where the storm calms down (wave packets 4 and 5).

The evolution of the mean effective stress (see in Figure 7(b)) highlights the partially drained behaviour of the soil. Both variables don't have the same amplitude of variation (see in Figures 7(b) and 7(a)). During a cycle, the major part of the loading is transferred to pore water pressure. Overpressure cannot dissipate totally before unloading. Hence, only a small part of the loading passes from pore water pressure to soil skeleton. A smaller skirt length involves that a greater part of the loading stresses the soil at the top of the caisson. The initial mean effective stress is greater but the deviatoric stress as well leading to greater plasticity and displacement of the caisson.

5.3 Permeability

Reducing permeability leads to a weaker dissipation of the pore water pressure and a build up of this pressure for the greatest loading amplitude ($\sigma_{v,cycl} = \sigma_{v,cycl,max}$, see in Figure 9(a)). The loading is essentially supported by the pore water pressure. As a consequence, the tendency of the mean effective stress is to evolve more slightly and the variation around this tendency is weaker. Then, the soil is not prone to rearrange and deform. As a consequence, the displacement is quite the same (see in Figure 8(b)).

On the other hand, a greater permeability involves a greater variation of both mean effective and deviatoric stresses. Then the soil is submitted to a greater loading and its deformation is larger (see in Figure 8(b)).

6 CONCLUSIONS

The main purpose of this paper was to capture the main features of the cyclic loading of suction caissons modelled using the Prevost's model. A parametric study was carried

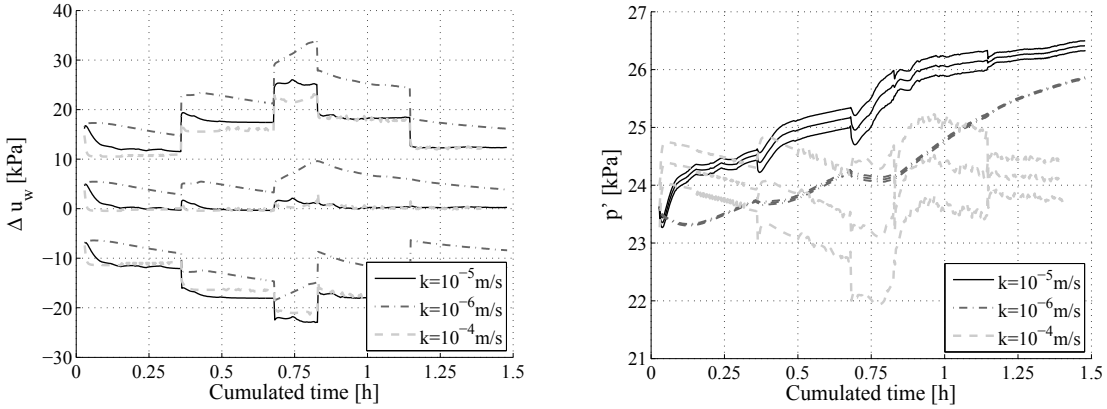

(a) Variations in water pore pressure : mean tendency and envelop curve.

(b) Mean effective stress : mean tendency and envelop curve.

Figure 9: Influence of the permeability : evolution of pore pressure variation and mean effective stress with time at point 1.

out to better understand the influence of the key factors such as permeability and skirt length. Experimental results are not really scattered in literature because of commercial purpose. Then only numerical simulations are presented in this paper.

Couplings between soil plasticity and flow around the caisson are not easy to predict, *a priori*. In the case presented here, the pore water pressure, unable to dissipate, sustains the main part of the cyclic loading. Then the soil skeleton is only submitted to a fraction of the total cyclic loading and its deformation is weaker than for a drained loading. Two parameters are shown to affect the total displacement : the skirt length (the greater the length the smaller the displacement) and the permeability. The role of the latter depends on several factors. It was shown in this case than a 10^1 times greater permeability entails a greater displacement whilst a 10^{-1} times smaller permeability nearly doesn't influence the displacement.

This paper was a first step to an accurate modelling of suction caissons. The future work will focuses on the improvement of simulations. Contact elements should be added to take into account the sliding between the soil and the caisson. Improvements of the model are also necessary to represent the cyclic path of the soil more accurately and to overcome "local failures". Finally a switch to 3D is unavoidable to take into account the horizontal load transmitted to the soil.

REFERENCES

[1] Stuyts, B. and Irvine, J. and Cathie, D., Assessing the stability of tripod foundations for offshore win turbines under cyclic loading. *Proc. of he the 8th Int. Conf. on Structural Dynamics, EURODYN 2011*, (2011) 3482-3489

[2] Senders, M., Suction caissons in sand as tripod foundations for offshore wind turbines.

Thesis, University of Western Australia, (2008)

[3] Byrne, B.W and Houlsby, G.T., Experimental investigations of response of suction caissons to transient vertical loading. *J. of the Geotech. and Geoenv. Eng.*, (2002) **128**:926-939

[4] Houlsby, G.T., Suction caissons for wind turbines. *Proceedings of the international symposium on frontiers in offshore geotechnics*, (2005) 75-94

[5] Houlsby, G.T. and Kelly, R.B. and Huxtable, J. and Byrne B.W, Field trials of suction caissons in sand for offshore wind turbine foundations *Géotechnique*, (2006) **56**:3-10

[6] Taiebat, H.A., Three dimensional liquefaction analysis of offshore foundations. *Thesis*, University of Sydney, (1999)

[7] Prevost, J.H., A simple plasticity theory for frictional cohesionless soils. *Soil Dynamics and Earthquake Engineering*, (1985) **4**:9-17

[8] Yang,Z. and Elgamal, A., Multi-surface cyclic plasticity sand model with lode angle effect. *Geotechnical and Geological Engineering*, (2008) **26**:335-348

[9] Prevost, J.H. and Hughes, T.J.R. and Cohen, M.F., Analysis of gravity offshore structure foundations *Journal of Petroleum Technology*, (1980) **32**:199-209

[10] Ishihara, K. and Tatsuoka, F. and Yasuda, S. , Undrained deformation and liquefaction of sand under cyclic stress. *Soils and Foundations*, (1975) **15**:29-44

[11] Ibsen, L.B. and Jakobsen, F.R. , *Lund sand No 0, Data Report 8401, 8402, 8801 & 8901*, (1996) Soil Mechanichs Laboratory, Aalborg University, Denmark

[12] Hyodo, M. and Hyde, A.F.L. and Aramaki, N. and Nakata, Y., Undrained monotonic and cyclic shear behaviour of sand under low and high confining stresses. *Soils and Foundations*, (2002) **42**:63-76

[13] Rahman, M.S. and Seed, H.B. and Booker, J.R., Pore pressure development under offshore gravity structures. *J. of the Geotech. Eng. Div.* ASCE, (1977) **103**:1419-1436

[14] Lee, K.L. and Focth, J.A., Liquefaction potential at Ekofisk tank in North Sea *J. of the Geotech. Eng. Div.* ASCE, (1975) **101**:1-18

[15] DNV, Foundations, classification notes No 30.4, - Foundations, Det Norske Veritas, Høvik, Norway, (1992)

[16] Ibsen, L.B., The mechanism controlling static liquefaction and cyclic strength of sand *Proc. of Int. Workshop on Physics and Mechanics of Soil Liquefaction*, Baltimore, (1998) Soil Mechanichs Laboratory, Aalborg University, Denmark